agriculture

MDPI

Article

Calibration and Experimental Validation of DEM Rolling Friction Parameters for Peanut Seeds Classified by Pod Position

Weizhi Feng [1], Xinping Jia [1], Xinyan Ou [1], Chunrong Li [1], Min Liu [1], Dongyan Huang [1], Gang Wang [2], Daping Fu [1], Wei Song [1] and Jingli Wang [1,*]

[1] College of Engineering and Technology, Jilin Agricultural University, Changchun 130118, China
[2] College of Biological and Agricultural Engineering, Jilin University, Changchun 130021, China
* Correspondence: wangjingli@jlau.edu.cn

Abstract

A single rolling friction coefficient in discrete element method (DEM) simulations cannot represent differences in rolling resistance among morphology-based peanut seed classes. After shelling, Silihong peanut seeds were classified as upper, middle, or lower based on seed-shape features associated with compression by neighboring seeds. Physical and contact properties were measured, and multi-sphere models were constructed using class-specific geometries and a common geometry based on dimensions weighted by a prescribed 1:2:1 seed-number ratio. Calibration against the measured static angle of repose of 22.280° yielded a baseline seed–seed rolling friction coefficient of 0.02552; rerunning the simulation with this coefficient reproduced the calibration target with a relative error of 0.485%. Shape corrections derived from aspect ratios and single-seed critical angles were 1.1046, 0.9687, and 0.9579, giving class-specific coefficients of 0.02819, 0.02472, and 0.02445 while preserving their weighted mean. At a drum speed of 15 r/min, the three particle models produced similar overall dynamic angles of repose. Coupled simulations yielded qualified, multiple, and missed seeding indices of 92.2%, 6.7%, and 1.1%, respectively, close to the bench-test values; all three mean indices met the cited technical requirements. The parameter set and calibration procedure provide a case-specific reference for the tested Silihong seed batch, particle representation, moisture content, and metering conditions.

Keywords: Silihong peanut; discrete element method; rolling friction; multi-sphere model; angle of repose; vacuum seed metering; EDEM–Fluent coupling

1. Introduction

Peanut (*Arachis hypogaea* L.) is an important oilseed crop in China, with national production of approximately 19.23 million tonnes in 2023 [1]. The self-sufficiency rate for edible vegetable oil was approximately 35% in the same period [2], highlighting the need to increase domestic oilseed production. Silihong is a specialty peanut cultivar widely grown in northeastern China. Its seeds vary in size and have irregular shapes. In vacuum seed-metering devices, they slide, roll, and tumble under gas–solid interactions. Because the motion and forces acting on individual seeds are difficult to observe directly, discrete element simulations can help investigate these processes. Their reliability depends on the contact parameters and particle representation. Calibrating rolling friction for morphology-based seed classes associated with pod positions is therefore relevant to vacuum seed-metering simulations.

Check for updates

Academic Editor: Ju-Seok Nam

Received: 23 September 2026
Revised: 28 October 2026
Accepted: 2 November 2026
Published: 4 November 2026

Copyright: © 2026 by the authors. Licensee MDPI, Basel, Switzerland. This article is an open access article distributed under the terms and conditions of the Creative Commons Attribution (CC BY) license.

The discrete element method (DEM), introduced by Cundall and Strack [3], is widely used to investigate the motion of agricultural particles and the forces acting on them. It solves the equations of motion for individual particles. Tsuji et al. [4] combined DEM with computational fluid dynamics (CFD) to analyze particle–airflow interactions. In DEM, seeds are commonly represented by spheres or multi-sphere particles, and an effective rolling friction coefficient is used to represent resistance to rolling [5,6]. This coefficient affects predicted packing and flow, but it is difficult to measure directly and depends on the particle geometry, contact model, and measurement procedure [6]. Calibrated values are therefore not universally transferable between studies. Inverse calibration against macroscopic responses, such as the angle of repose, has been applied to a range of agricultural materials, including cotton seeds [7], squash seeds [8], Chinese cabbage seeds [9], sunflower seeds [10], wheat seeds [11], *Leymus chinensis* seeds [12], rice seeds [13], and maize seeds [14]. Particle representations include single spheres, polyhedra, and multi-sphere models, while calibration methods include orthogonal experimental designs, response surface methods, and convolutional neural networks [15].

Seed morphology, including triaxial dimensions and aspect ratio, affects rolling behavior, packing, and flow. Kodicherla et al. [16] quantified the effect of particle morphology on the angle of repose using DEM, and Doan et al. [17] distinguished the contributions of rolling friction and cohesion at the contact scale. Nevertheless, calibration studies generally assign one rolling friction coefficient to a material. For example, Wang et al. [18] calibrated an alfalfa seed model using angle-of-repose tests, while Xu et al. [19] developed an olive fruit model and analyzed contact-parameter sensitivity. Neither study distinguished morphological classes within the material. Morphology-based assignment of class-specific rolling friction parameters therefore warrants further investigation.

Calibrated parameters are often assessed by reproducing angles of repose and seed-metering responses. Du et al. [20] measured the angle of repose by automatically extracting simulated particle coordinates, reducing the subjectivity of manual line selection. Pourandi et al. [21] developed a framework that distinguishes the effects of sliding friction, rolling friction, and the Froude number on the dynamic angle of repose. Orefice et al. [22] noted that a single free-surface measure cannot characterize the entire flow response. Many calibration studies assess reproduction of a static angle of repose, with less attention to dynamic conditions. For seed-metering devices, Xu et al. [23], Sun et al. [24], and Xing et al. [25] used coupled CFD–DEM simulations to optimize vegetable, maize, and rice seed meters, respectively. Lei et al. [26] compared simulations with bench tests for a centralized pneumatic seed-metering device, in which airflow is concentrated in suction-hole channels. Wang et al. [27] simulated and measured the suction force on individual ellipsoidal seeds. For peanut seeds, Guo et al. [28] investigated an auxiliary air-suction seed-filling structure, Diao et al. [29] measured physical properties and developed multi-sphere models, and Wu et al. [30] calibrated DEM parameters using the angle of repose. These peanut studies did not assign rolling friction parameters to morphology-based seed classes.

Although DEM calibration is well established for agricultural particles, few studies have accounted for pod-position-related morphology when calibrating peanut rolling friction or evaluated the resulting parameters using both dynamic and seed-metering responses. This study develops a class-specific calibration procedure using shape corrections. A baseline seed–seed rolling friction coefficient is obtained by parameter scanning and response inversion against the static angle of repose. The model is then rerun with the calibrated coefficient to check whether it reproduces the calibration target. Shape corrections are then constructed from aspect ratios and class differences in single-seed critical angles on a tough resin plate, preserving the weighted mean rolling friction coefficient. The parameters are subsequently evaluated using a fixed-speed drum test and a comparison of coupled

simulations with bench tests. The resulting parameters are specific to the tested seeds and operating conditions.

2. Materials and Methods

2.1. Seed Material, Classification, and Physical Property Measurements

Silihong peanut seeds were purchased from a seed market in Jilin, China. The experiments were conducted in 2026. Seeds were stored in sealed polyethylene bags at 20 ± 2 °C; physical and contact-property measurements were completed within 48 h of opening the bags. Before testing, seeds were held at 20 ± 2 °C for 2 h. Moldy, damaged, and shriveled seeds were removed. The experimental material consisted of shelled seeds. After shelling, seeds from multi-seed pods were classified as upper, middle, or lower based on seed-shape features associated with compression by neighboring seeds (Figure 1). These morphological features defined the classes; individual seed positions within the pod were not verified before shelling. A typical four-seed pod contains one upper seed, two middle seeds, and one lower seed. The two middle seeds occupy distinct positions but belong to the same morphological class. Seeds from single-seed pods lack compression by neighboring seeds and were not used to define these classes. Each class comprised three groups of 100 randomly selected seeds for triaxial measurements. Measurements were performed in the Engineering Training Center laboratory at Jilin Agricultural University.

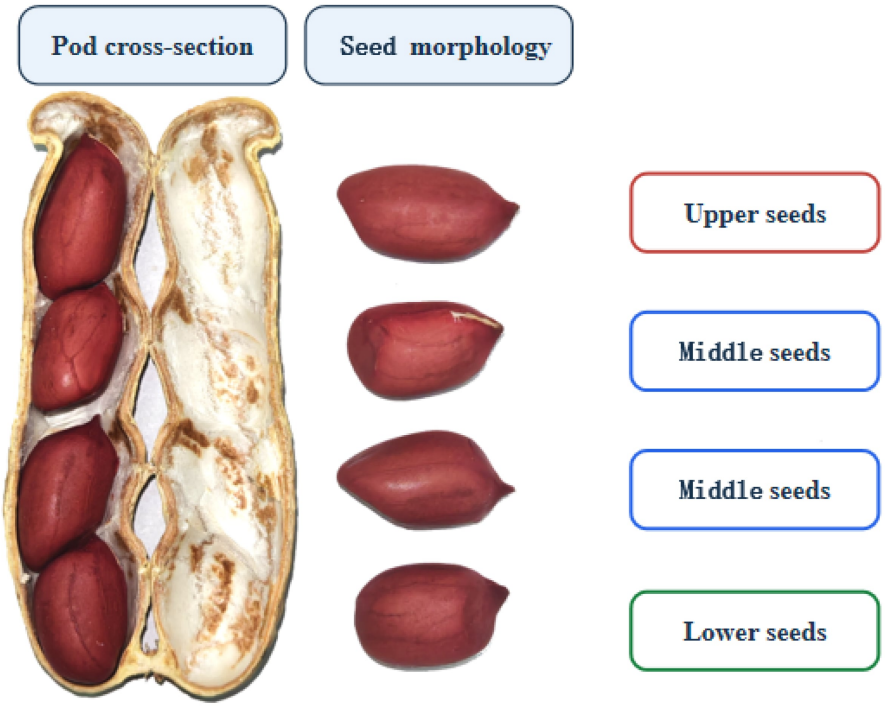


Figure 1. Morphology-based seed classes labeled upper, middle, and lower with reference to a typical four-seed pod. The two middle positions in the pod are distinct positions within the same middle class. Classification was based on compression-related morphology after shelling; individual seed positions were not verified before shelling.

A prescribed upper:middle:lower seed-number ratio of 1:2:1 was used in the physical static and dynamic angle-of-repose tests, bench tests, and corresponding simulations. This ratio represents the composition of a typical four-seed pod and ensures that the physical tests and simulations use the same mixture composition. It does not represent the natural frequency distribution of seed counts per pod or seed classes. Pods were sources of seeds rather than sampling or analytical units.

The triaxial dimensions were defined as maximum length (L), width (B), and thickness (T), as shown in Figure 2. Individual seeds were measured using a digital caliper (Guilin Guanglu Measuring Instrument Co., Ltd., Guilin, China; accuracy: 0.02 mm). Means and sample standard deviations (SDs) were calculated from 300 individual seeds per class. The 100-seed mass was measured three times per class using a BSA-series electronic balance (Sartorius, Göttingen, Germany; accuracy: 0.01 g), with 100 seeds counted for each weighing. The statistical unit was an individual seed for dimensions and one 100-seed weighing for mass. Sample SDs used the $n - 1$ denominator. Table 1 reports class means ± SD; the weighted-mean row lists representative values calculated from the three class means using 1:2:1 weights. Upper seeds had the greatest length and aspect ratio, lower seeds were thicker, and middle seeds were intermediate.

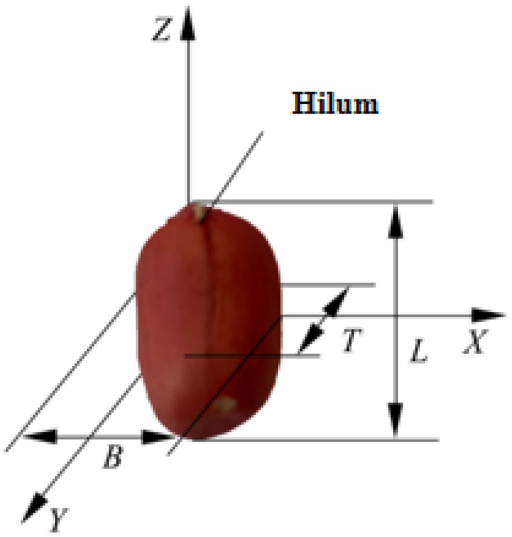


Figure 2. Definition of the triaxial dimensions of a Silihong peanut seed.

Table 1. Measured physical properties of Silihong peanut seeds.

Seed Class	Length (mm)	Width (mm)	Thickness (mm)	100-Seed Mass (g)
Upper	15.15 ± 1.10	8.47 ± 0.52	7.62 ± 0.40	47.34 ± 0.54
Middle	14.03 ± 0.73	8.39 ± 0.42	7.67 ± 0.46	45.59 ± 0.33
Lower	13.94 ± 0.99	8.38 ± 0.47	8.00 ± 0.44	48.63 ± 1.38
Weighted mean	14.29	8.41	7.74	46.79

Seed density was determined by water displacement. Seeds of known mass were submerged in distilled water in a graduated cylinder, and the volume increase after air bubbles had been removed was used to calculate density. The mean density was 1018.2 kg m^{-3}. Moisture content was measured by drying seeds in a DHG-9040 oven (KENTON, Guangzhou, China) at 105 °C until successive mass measurements were essentially unchanged. Wet-basis moisture content, calculated as mass loss divided by initial seed mass, was 4.18%. Physical and contact properties were measured at this moisture condition. Table 1 summarizes the dimensions and 100-seed mass.

Elastic properties were determined from compression tests. Intact upper, middle, and lower seeds were compressed individually along the length, width, and thickness directions using a TH-8201S universal testing machine (Suzhou Tuobo Machinery Equipment Co., Ltd., Suzhou, China). Loading proceeded at 5 mm/min until the force–displacement curve showed a clear inflection point. Initial cross-sectional dimensions and representative triaxial

dimensions were used to convert the curves to stress–strain relationships. Young's modulus was calculated over 20–60% of peak stress using Equation (1). The initial region affected by surface irregularity and contact seating was excluded. This yielded E = 40.23 MPa. Because lateral deformation was difficult to measure simultaneously, Poisson's ratio, $\nu = 0.362$, was taken from a study of the same cultivar [30]. Equation (2) then gave a shear modulus of G = 14.77 MPa.

$$E = \sigma/\varepsilon \tag{1}$$

$$G = \frac{E}{2(1+\nu)} \tag{2}$$

where E is the elastic modulus (Young's modulus; MPa), σ is the compressive stress (MPa), ε is the axial strain (dimensionless), G is the shear modulus (MPa), and ν is Poisson's ratio (dimensionless).

2.2. Contact Property Measurements and Boundary Parameters

2.2.1. Coefficient of Restitution

The coefficient of restitution was measured using a free-fall rebound apparatus and high-speed imaging [31] (Figure 3). An S1310 camera (Hefei Zhongke Junda Vision Technology Co., Ltd., Hefei, China) recorded at 240 frames/s with a resolution of 1280 × 720 pixels and a shutter speed of 1/1000 s. The camera was approximately 600 mm from the motion plane, with its optical axis normal to that plane and a vertical field of view of approximately 400 mm. A scale in the trajectory plane provided pixel-to-length calibration, giving approximately 0.56 mm per pixel and an estimated rebound-height uncertainty of ±1 mm. Seeds with dimensions close to the class means were held with tweezers, with the long axis parallel to the impact surface, and released from 300 mm without deliberately imparting rotation. The camera position was fixed, and background grid lines were used to maintain the release position. A tough resin plate represented seed–resin contact, and a seed-covered plate represented seed–seed contact. Trials were excluded if the trajectory was obscured, left the measurement plane, or extended beyond the image. Ten valid trials were obtained. For each trial, the coefficient was calculated using Equation (3) as the square root of the ratio of rebound height to release height; the ten coefficients were then averaged arithmetically. The seed–seed and seed–resin coefficients were 0.414 and 0.516, respectively.

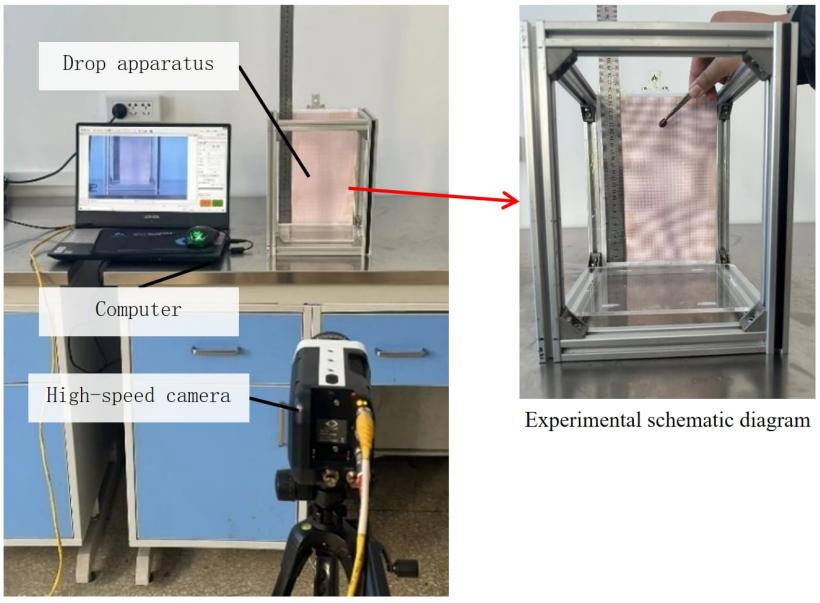


Figure 3. Drop–rebound apparatus for measuring the coefficient of restitution.

$$e = \sqrt{h_1/h_0} \quad (3)$$

where e is the coefficient of restitution (dimensionless), h_1 is the maximum rebound height (mm), and h_0 is the release height (mm).

2.2.2. Coefficient of Static Friction

Static friction was measured with a custom-built inclined plane and a miniature digital angle gauge [31] (Figure 4). Seeds were placed with their long axes parallel to a tough resin plate, and the inclination was gradually increased. Samples that tended to roll were excluded. The angle at the onset of sliding was substituted into Equation (4), giving a seed–resin static friction coefficient of 0.472. Repeating the procedure on a surface of closely packed seeds gave a seed–seed coefficient of 0.376. The seed-covered plate maintained contact with a seed surface over the sliding distance and reduced substrate and edge effects.

$$\mu_s = tan\varphi \quad (4)$$

where μ_s is the coefficient of static friction (dimensionless), and φ is the angle between the inclined plane and the horizontal at the onset of seed sliding, referred to as the friction angle (°).

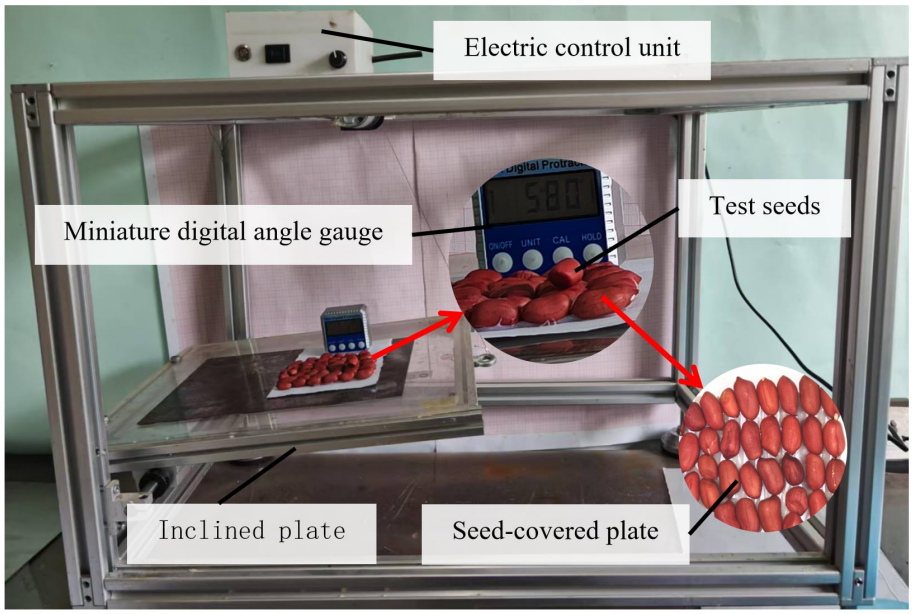


Figure 4. Custom-built inclined-plane apparatus.

2.2.3. Rolling Friction Measurements and Model Inputs

Single-seed critical angles were measured by slowly inclining a tough resin plate until a seed began to roll or tumble. The inclination at that point was recorded as the critical angle. Thirty seeds were tested per class, giving a standard error below 0.62° for each class mean. Tests on a fixed seed-covered plate, with 15 seeds per class, were used only as a cross-check.

Critical angles depend on seed shape, orientation, and contact conditions and cannot be entered directly as DEM rolling friction coefficients. Resin-plate critical angles were used to construct relative shape corrections, while measured seed–seed rolling behavior informed the scan range. Together with ranges reported for peanut and other granular materials [18,29,30], these measurements motivated a coarse seed–seed rolling friction scan from 0.01 to 0.25, followed by a fine scan. The seed–seed restitution coefficient of 0.414 and static friction coefficient of 0.376 were measured using the seed-covered plate procedures in

Sections 2.2.1 and 2.2.2. The baseline rolling friction coefficient, $\mu_0 = 0.02552$, was calibrated against the static angle of repose (Sections 2.4 and 3.1), rather than measured directly.

The seed–resin rolling friction coefficient was obtained by inverse simulation of the measured resin-plate critical angles. A single-seed model was constructed in Altair EDEM 2024 using the 29-sphere weighted mean geometry. Five rolling friction levels, $\mu = 0.02$, 0.05, 0.08, 0.11, and 0.14, were tested with three initial configurations per level. Their mean critical angles were 5.56°, 7.22°, 9.32°, 11.62°, and 13.94°, respectively. Within $0.02 \leq \mu \leq 0.14$, the fitted relationship was $\theta = 120.63\mu^2 + 51.23\mu + 4.44$ ($R^2 = 0.9996$). Inverting this relationship for the measured class means gave coefficients of 0.1387, 0.1184, and 0.1171 for upper, middle, and lower seeds. Their 1:2:1 weighted mean, 0.12314, was adopted for seed–resin rolling friction.

The density, Poisson's ratio, and shear modulus of tough resin were assigned provisional engineering values [32]. Table 2 lists the material and contact parameters.

Table 2. Basic material and contact parameters used in the DEM model.

Material/Contact	Parameter	Value
Peanut seed	Density (kg m^{-3})	1018.2
	Young's modulus (MPa)	40.23
	Poisson's ratio	0.362
	Shear modulus (MPa)	14.77
Seed–seed	Coefficient of restitution	0.414
	Coefficient of static friction	0.376
	Rolling friction coefficient (coarse-scan range)	0.01–0.25
Seed–tough resin	Coefficient of restitution	0.516
	Coefficient of static friction	0.472
	Rolling friction coefficient (critical-angle inversion)	0.12314
Tough resin wall	Density (kg m^{-3})	1050
	Poisson's ratio	0.35
	Shear modulus (MPa)	800

2.3. Particle Geometries and Contact Model

The weighted mean dimensions in Table 1 (14.29 × 8.41 × 7.74 mm) were the target for the common particle geometry. A representative seed with dimensions closest to these values was scanned using a KSCAN-E 3D laser scanner (SHINING 3D Tech Co., Ltd., Hangzhou, China). The resulting STL geometry was filled with 29 spheres. This representation was selected to balance geometric fidelity with computational cost while limiting the effect of geometric simplification on the simulated response. Figure 5 shows the class-specific and weighted mean geometries. Multi-sphere filling did not retain seed-coat irregularities or local contact curvature. The geometries were imported into Altair EDEM 2024, using the Hertz–Mindlin (no slip) contact model and a time step of 20% of the Rayleigh time step. This contact model describes nonlinear elastic normal contact and tangential friction, but not explicit viscoelasticity, plasticity, adhesion, or moisture films. The calibrated values are effective parameters for the tested conditions.

Three models were compared in the rotating-drum apparatus, each with 300 seeds. In the class-specific mean-geometry model (CMG), one scanned seed with dimensions closest to each class mean represented that class. The mixture contained 75 upper, 150 middle, and 75 lower particles, with uniform seed–seed rolling friction. This model retained between-class shape differences but did not reproduce individual seed contours. The mean-geometry model with uniform rolling friction (MGU) used the common weighted mean geometry for

all particles. The mean-geometry model with class-specific rolling friction (MGC) used the same geometry as MGU, but assigned class-specific seed–seed coefficients. These drum models and the 300-seed metering simulations are distinct from the 380-seed static calibration.

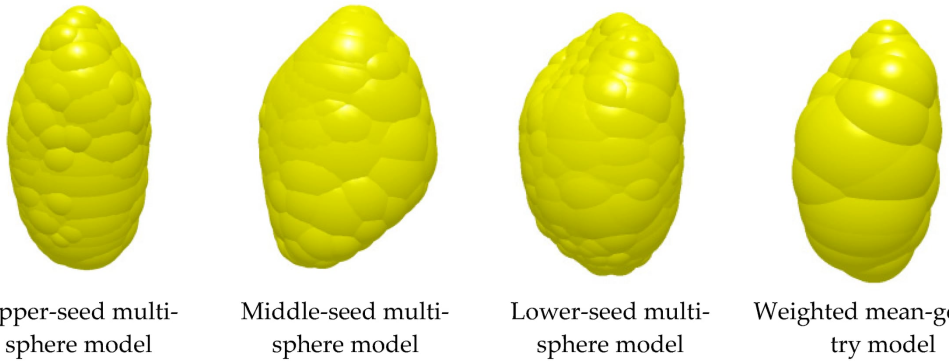


Figure 5. DEM geometries of upper, middle, and lower Silihong peanut seeds and the weighted mean-geometry model.

Sphere-count sensitivity of the selected representation was examined using five simulation runs for each of eight models containing 16, 18, 21, 23, 27, 29, 32, and 35 spheres. The rolling friction coefficient was fixed at $\mu_r = 0.11$ for this sensitivity test; this was not the final calibrated coefficient adopted in the study. Table 3 reports the critical rolling-angle mean, sample SD, and signed percentage deviation from the five-run 29-sphere mean.

Table 3. Sensitivity of the critical rolling angle to sphere count.

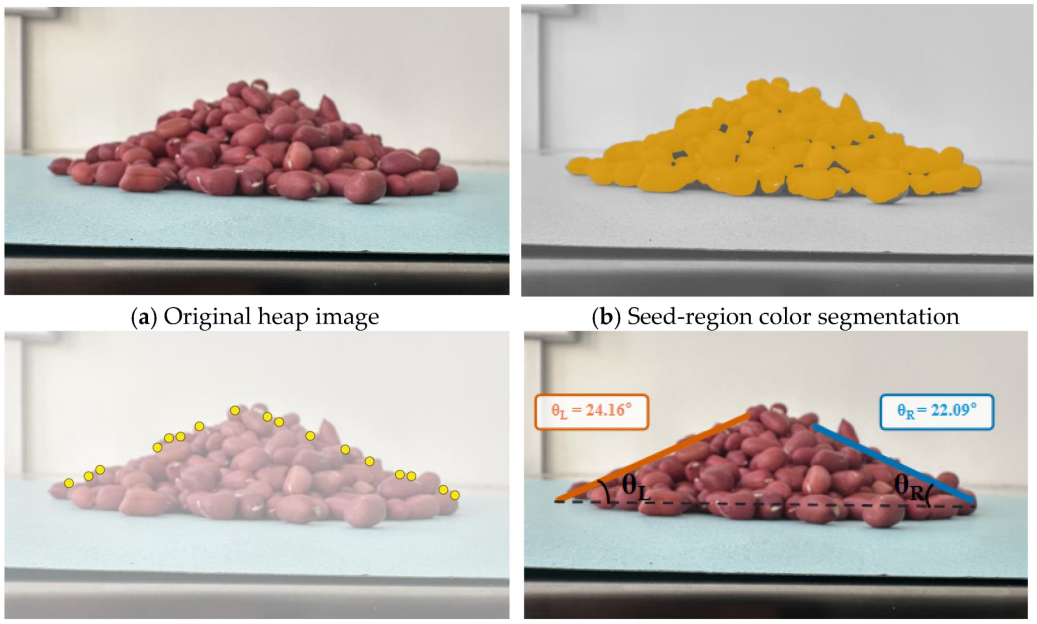
Sphere Count	Mean (°)	SD (°)	Deviation from 29 Spheres (%)
16	10.77	0.100	−7.31
18	10.99	0.095	−5.42
21	11.28	0.077	−2.93
23	11.43	0.074	−1.64
27	11.57	0.064	−0.43
29	11.62	0.068	0.00
32	11.69	0.068	+0.60
35	11.59	0.065	−0.26

Mean critical rolling angles for 27, 29, 32, and 35 spheres were 11.57°, 11.62°, 11.69°, and 11.59°, respectively. Deviations from the 29-sphere mean were −0.43%, +0.60%, and −0.26% for 27, 32, and 35 spheres. The small changes near 29 spheres support retaining the selected representation for the tested critical rolling-angle response and sphere-count range.

2.4. Static Angle-of-Repose Measurement and Simulation Calibration

The static angle of repose was measured by lifting a cylinder at 0.05 m/s, allowing seeds to form a heap on a horizontal base. The seed composition followed the prescribed 1:2:1 seed-number ratio defined in Section 2.1. Side views were photographed with the camera optical axis horizontal and aligned with the heap center. A Python 3.12.10 program identified seed regions by color segmentation, extracted the free surface from 36 equally spaced horizontal sampling intervals, and fitted the left and right slopes separately. Their angles were averaged. Photographs were retained when the profile-fit R^2 was at least 0.95 and the left–right slope-angle difference did not exceed 5°. Thirty photographs met these criteria. The 4000 × 3000-pixel camera was approximately 800 mm from the heap; calibration against the apparatus dimensions gave approximately 0.06 mm per pixel. Reported decimal

places reflect the numerical fitting output, while the between-photograph SD describes practical scatter. Figure 6 shows the processing procedure. The measured static target was 22.280° ± 2.964°, where SD describes variation among photographs due to heap formation and imaging.



(**a**) Original heap image (**b**) Seed-region color segmentation

(**c**) Free-surface profile extraction (**d**) Linear fits to the left and right slopes

Figure 6. Image-processing and slope-fitting procedure for the static angle of repose: (**a**) original heap image; (**b**) seed-region color segmentation; (**c**) free-surface profile extraction; and (**d**) linear fits to the left and right slopes.

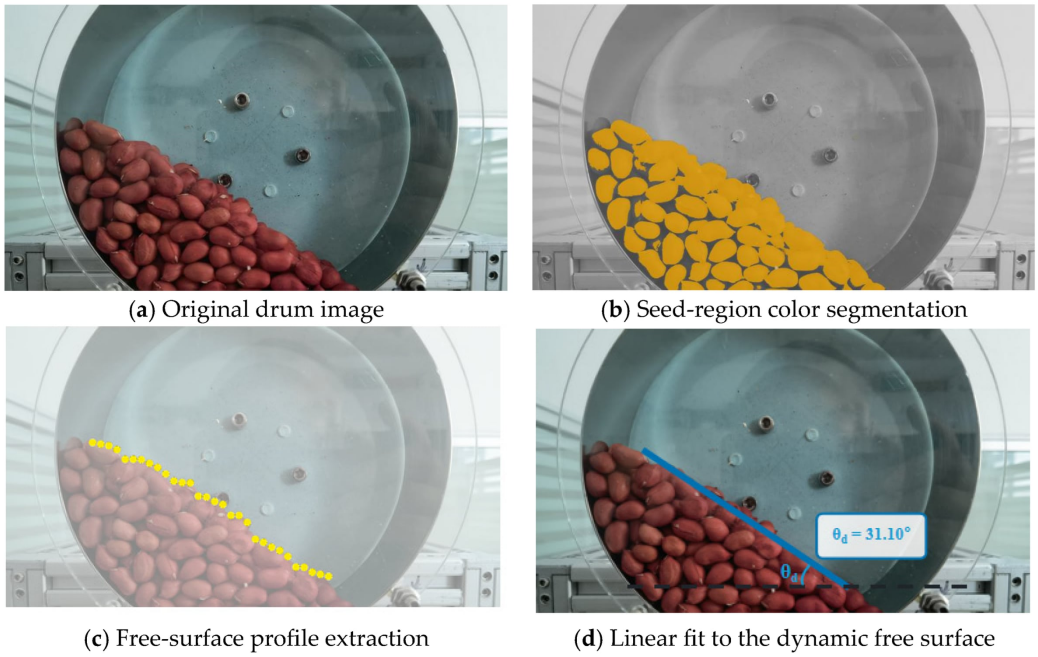
The coarse scan, fine scan, and subsequent simulation check were conducted in EDEM. After calibration, the model was rerun with the calibrated coefficient to check whether it reproduced the measured static angle of repose. A coarse scan tested ten rolling friction levels over 0.01–0.25. The response increased overall but was not monotonic, and the target of 22.280° fell within the lower response range corresponding to 0.01–0.03. The fine scan therefore covered 0.018–0.036 in increments of 0.002. At each of the ten levels, three initial configurations were defined by horizontal and vertical centroid offsets within the container cross-section: (0, 0), (0.4, −0.3), and (−0.4, 0.3) mm. Each configuration was run five times, giving 15 runs per level and 150 runs in total. Each run used 380 weighted mean-geometry particles introduced in one batch. The simulated cylinder was also lifted at 0.05 m/s. Particles fell and accumulated during 1–3 s; the total duration was 4.0 s, including approximately 1 s of settling. Heap profiles were extracted over the stable 3.6–4.0 s interval from the ±X and ±Y views. Profile extraction followed the physical-image procedure. A simulation run was retained only if the minimum R^2 across the four views exceeded 0.95 and the maximum left–right slope-angle difference was below 5°. The four-view mean was the response for that run; views were not counted as separate replicates. Relative error against the measured target was calculated using Equation (5):

$$\delta = \frac{|\theta_{sim} - \theta_{meas}|}{\theta_{meas}} \times 100\% \quad (5)$$

where δ is the relative error (%), θ_{sim} is the simulated static angle of repose combined from four views (°), and θ_{meas} is the measured static target (°).

2.5. Dynamic Angle-of-Repose Measurement and Statistical Analysis

The dynamic angle of repose was measured from ten side-view photographs of a drum with an internal diameter of 150 mm, an axial width of 30 mm, and a fill height of approximately 50 mm, rotating at 15 r/min. The physical test and corresponding simulations used the prescribed 1:2:1 seed-number ratio defined in Section 2.1. A single free-surface slope in the direction of rotation was extracted. Segmentation and fitting followed the static-image procedure (Figure 7). The measured dynamic target was 30.362° ± 2.457°, where SD describes variation among photographs.



(**a**) Original drum image (**b**) Seed-region color segmentation

(**c**) Free-surface profile extraction (**d**) Linear fit to the dynamic free surface

Figure 7. Image-processing and free-surface fitting procedure for the dynamic angle of repose: (**a**) original drum image; (**b**) seed-region color segmentation; (**c**) free-surface profile extraction; and (**d**) linear fit to the dynamic free surface.

Dynamic simulations used the physical drum geometry and speed, with 300 seeds per run and three runs per model. After the bed formed, a straight line was fitted to the free surface in the direction of rotation. The response for each run was the mean angle over 6.0–10.0 s, corresponding to one complete revolution. Individual framewise angles were not treated as independent replicates. Results are reported as means ± sample SDs with 95% confidence intervals (CIs). One-way analysis of variance (ANOVA) and Welch's tests were performed using SciPy in Python 3.12.10. Each replicate run was one statistical unit; multiple views were used only for geometric extraction.

3. Results

3.1. Static Angle-of-Repose Calibration

Static angle-of-repose calibration used the weighted mean-geometry multi-sphere model based on the 1:2:1 seed-number weighting. Figure 8 shows the simulated heap in the +X view, containing 380 particles and 11,020 constituent spheres, together with the fitted left and right free surfaces. The same four-view extraction and slope-fitting procedure was used for the fine scan and the simulation check. The calibration target was the measured static angle of repose of 22.280° ± 2.964°, with the latter value representing the sample standard deviation among photographs.

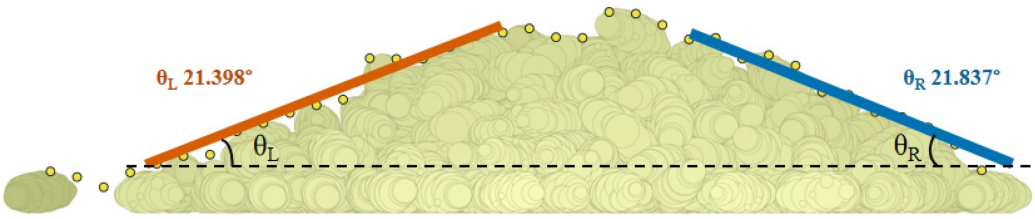


Figure 8. Simulated heap of mean-geometry multi-sphere particles and free-surface fits.

The fine scan comprised ten levels with 15 runs per level. Before screening, the level means increased overall but showed local nonmonotonic changes. Applying the four-view criteria in Section 2.4 retained 109 runs and excluded 41: 19 failed only the R^2 criterion, 14 failed only the slope-angle criterion, and eight failed both. The overall mean was 22.513° (SD 1.338°, n = 150) before screening and 22.567° (SD 1.194°, n = 109) after screening. A conditional randomization test holding the total number of exclusions fixed did not detect an association between exclusion status and friction level (Pearson $\chi^2 = 11.043$; Monte Carlo $p = 0.302$, 300,000 permutations). This result does not establish the absence of an association. Table 4 reports the retained and excluded counts and the means and between-run sample SDs before and after screening. Screening depended on image quality, not proximity to the target angle. Relative errors were calculated from screened level means and the target of 22.280° using Equation (5). The screened means at the ten levels were fitted as:

$$\theta = 165.4990\mu_r + 18.0563,\ R^2 = 0.9768 \quad (6)$$

where θ is the four-view mean static angle of repose (°), μ_r is the dimensionless seed–seed rolling friction coefficient, and R^2 is the coefficient of determination. The fit used the ten screened level means in Table 4.

Table 4. Fine-scan statistics before and after quality screening.

μ_r	Retained/Excluded	Before Screening: Mean ± SD (°)	After Screening: Mean ± SD (°)	Absolute Difference from Target (°)	Relative Error (%)
0.018	11/4	21.172 ± 0.774	20.992 ± 0.636	1.288	5.78
0.020	9/6	21.950 ± 1.219	21.380 ± 1.053	0.900	4.04
0.022	10/5	21.304 ± 0.981	21.604 ± 0.759	0.676	3.03
0.024	13/2	22.476 ± 1.077	22.326 ± 0.782	0.046	0.21
0.026	10/5	22.640 ± 0.795	22.350 ± 0.495	0.070	0.31
0.028	9/6	21.970 ± 1.204	22.600 ± 0.706	0.320	1.44
0.030	15/0	23.027 ± 0.214	23.027 ± 0.214	0.747	3.35
0.032	10/5	22.541 ± 1.273	23.061 ± 1.062	0.781	3.51
0.034	10/5	23.701 ± 0.616	23.801 ± 0.613	1.521	6.83
0.036	12/3	24.346 ± 1.071	24.106 ± 0.878	1.826	8.20

Substituting the measured target of 22.280° into Equation (6) gave 0.025521. The baseline seed–seed rolling friction coefficient was reported as $\mu_0 = 0.02552$, between the two levels closest to the target, 0.024 and 0.026 (Table 4).

Figure 9 shows the screened level means in Table 4 and the linear fit in Equation (6).

At $\mu_0 = 0.02552$, the four-view mean simulated angle was 22.388°, giving a relative error of 0.485%. The opposing X and Y view means were 21.238° and 23.538°, a directional difference of 2.3°. This simulation check used the calibration target and criteria without independent random initial states, so it was an internal consistency check rather than independent validation. Figure 10 shows the fitted profiles. The absolute difference from

the target was approximately 0.108°, compared with a between-photograph SD of 2.964° for the measured target. The small error in reproducing the target does not quantify uncertainty in μ_0.

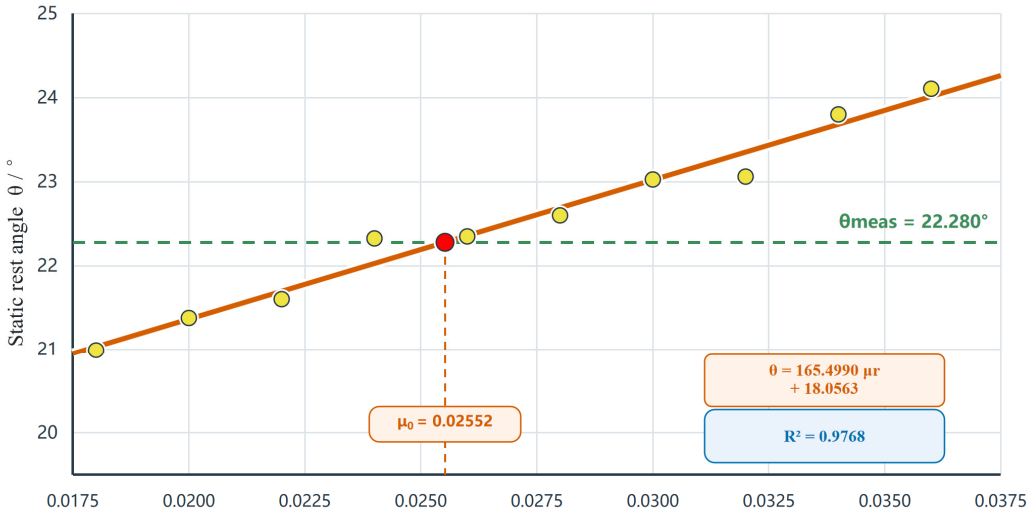
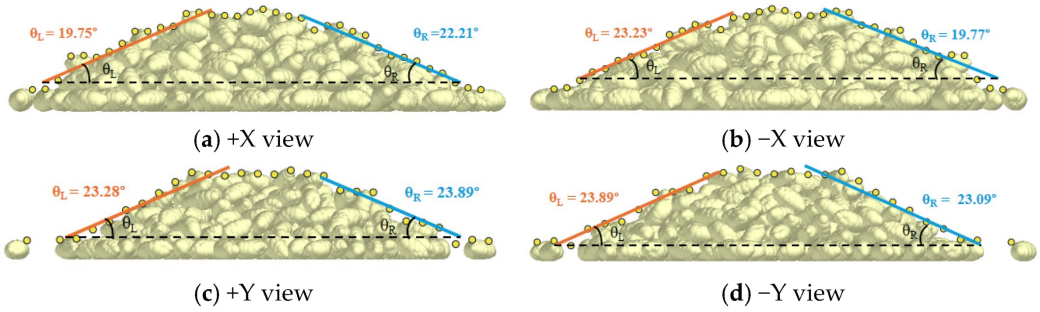


Figure 9. Relationship between seed–seed rolling friction and the static angle of repose.



(**a**) +X view (**b**) −X view

(**c**) +Y view (**d**) −Y view

Figure 10. Static angle-of-repose simulation check at a candidate rolling friction coefficient of 0.02552: (**a**) +X view; (**b**) −X view; (**c**) +Y view; and (**d**) −Y view.

3.2. Shape-Correction Candidates

Static calibration yielded an effective baseline coefficient, $\mu_0 = 0.02552$, for the mixed heap. A single macroscopic response cannot resolve class-specific resistance. Single-seed critical angles distinguished the three classes, but their shape dependence prevents their direct use as DEM rolling friction coefficients. Their relative class differences were therefore used to construct shape-correction coefficients, K_i, and redistribute the baseline resistance while preserving its weighted mean. Applying relative ratios from wall-contact tests to seed–seed contacts is a modeling assumption assessed indirectly through the subsequent dynamic tests.

Thirty seeds per class were tested on tough resin and 15 per class on a fixed seed-covered plate. Mean resin-plate critical angles were 13.8700°, 12.2000°, and 12.0967° for upper, middle, and lower seeds, respectively (permutation ANOVA, $p = 0.00288$). Corresponding seed-covered-plate means were 8.0400°, 6.5400°, and 6.2067° ($p = 0.0115$). These class differences supported construction of shape corrections, although critical angles are not DEM rolling friction coefficients. Table 5 summarizes both surfaces.

Table 5. Single-seed critical angles on inclined plates.

Contact Surface	Class	Mean (°)	Standard Deviation (°)
Tough resin	Upper	13.8700	3.3619
Tough resin	Middle	12.2000	1.2424
Tough resin	Lower	12.0967	1.4099
Fixed seed-covered plate	Upper	8.0400	1.7776
Fixed seed-covered plate	Middle	6.5400	2.0993
Fixed seed-covered plate	Lower	6.2067	0.9765

The measured critical angles were first converted to dimensionless relative resistance among classes using Equation (7):

$$K_{tan,i} = \frac{tan\theta_i}{\frac{\sum_j w_j \, tan\theta_j}{\sum_j w_j}} \quad (7)$$

where θ_i is the measured mean critical angle for class i on the tough resin plate (°), w_j is the seed-number weight of class j (1, 2, or 1), and $K_{tan,i}$ is the dimensionless relative resistance of that class. In Equation (7), tan θ_i was used.

The resulting $K_{tan,i}$ values were 1.1052, 0.9677, and 0.9593 for upper, middle, and lower seeds, respectively, with a 1:2:1 weighted mean of 1.

The relative-resistance ratios describe class differences without explicitly relating them to morphology. A shape relationship was therefore fitted within the present dataset. The aspect ratio λ_i was the arithmetic mean of individual L/B ratios in class i. Values were 1.7952, 1.6781, and 1.6684 for upper, middle, and lower seeds, with a weighted mean of $\lambda_0 = 1.7049$. The three candidate indices, L/B, B/T, and T/L, differed among classes. L/B was selected because its class ranking matched that of the critical angles and because this aspect ratio has a physical interpretation in rolling and tumbling. B/T and T/L remained supplementary descriptors. Regression through the origin in logarithmic space gave the following power-law relationship:

$$K_i = \left(\frac{\lambda_i}{\lambda_0}\right)^p, p = 1.9446 \quad (8)$$

where K_i is the dimensionless shape-correction coefficient for class i.

The exponent p was estimated by fitting the relative resistance in Equation (7) to aspect ratio. Taking logarithms of Equation (8) gives $\ln K_{tan,i} = p \ln(\lambda_i/\lambda_0)$. With $x_i = \ln(\lambda_i/\lambda_0)$ and $y_i = \ln K_{tan,i}$, the equal-weight least-squares slope through the origin was $p = \Sigma_i x_i y_i / \Sigma_i x_i^2$. The measured critical angles (Table 5) and aspect ratios gave $p = 1.9446$ and $R^2 = 0.9997$ in logarithmic space. The fit was based on only three class means and was applied only within the measured range. For small relative changes, a 1% change in L/B corresponds to an approximately 1.94% change in the correction coefficient. Values calculated using Equation (8) were divided by their weighted mean of 1.0009, yielding normalized coefficients of 1.1046, 0.9687, and 0.9579 with a 1:2:1 weighted mean of 1. These empirical quantities require reassessment for other samples.

To check consistency with critical-angle inversion, the three coefficients estimated in Section 2.2.3 were divided by their weighted mean. The same simulation data were also fitted as $\theta = 70.53\mu + 3.89$ ($R^2 = 0.9959$). Inverting the measured class angles with this linear relationship and normalizing by their weighted mean gave a second set of relative coefficients. Table 6 compares both sets with Equation (8).

Table 6. Consistency between the shape relationship and critical-angle inversion.

Class	Aspect Ratio, λ_i (L/B)	$K_{tan,i}$	K_i, Equation (8)	K_i, Quadratic Inversion	K_i, Linear Inversion
Upper	1.7952	1.1052	1.1046	1.1263	1.1469
Middle	1.6781	0.9677	0.9687	0.9614	0.9550
Lower	1.6684	0.9593	0.9579	0.9509	0.9431

The quadratic-inversion ratios differed from the shape-relationship values by −0.7% to +2.0%, and the linear-inversion ratios by −1.5% to +3.8%. These comparisons provide a consistency check with the coefficients obtained by inverting the measured critical angles; they do not independently validate the class-specific seed–seed coefficients.

The normalized shape corrections were applied to the static-calibration baseline, $\mu_0 = 0.02552$. Same-class contacts used $\mu_i = \mu_0 K_i$, and contacts between different classes used the geometric mean of their same-class coefficients:

$$\mu_{ij} = \mu_0 \sqrt{K_i K_j} \quad (9)$$

where μ_{ij} is the candidate rolling friction coefficient for a contact between classes i and j (dimensionless), μ_0 is the common seed–seed rolling friction candidate of 0.02552 obtained from static calibration, and K_i and K_j are the dimensionless shape-correction coefficients of the two classes.

Equation (9) gave same-class rolling friction coefficients of 0.02819, 0.02472, and 0.02445 and different-class coefficients of 0.02640, 0.02625, and 0.02458. Fixed seed-covered-plate results were used only as a cross-check. Table 7 reports the shape corrections, their 95% CIs, and the associated seed–seed coefficients. Intervals were estimated from 200,000 resampling iterations representing critical-angle sampling error. In each iteration, the SDs in Table 5 were divided by $\sqrt{n}$ to construct sampling distributions for the three means; p was refitted and K_i recalculated using Equation (8). Quantiles of the resulting distributions defined the intervals. The upper-seed interval was above 1 and did not overlap either the middle-seed interval or the lower-seed interval; both of the latter intervals were below 1. The results support the direction of the class corrections, subject to the uncertainty limitations in Section 4.3.

Table 7. Class-specific shape corrections and candidate seed–seed rolling friction coefficients.

Contact Type	K_i, Equation (8)	95% Confidence Interval of K_i	Candidate Seed–Seed Rolling Friction, μ_{ij}
Upper–upper	1.1046	1.0294–1.1775	0.02819
Middle–middle	0.9687	0.9467–0.9913	0.02472
Lower–lower	0.9579	0.9291–0.9881	0.02445
Upper–middle	—	—	0.02640
Upper–lower	—	—	0.02625
Middle–lower	—	—	0.02458

3.3. Dynamic Evaluation in a Drum at 15 r/min

Simulated dynamic angles were compared with measurements from a drum with an internal diameter of 150 mm, an axial width of 30 mm, a fill height of approximately 50 mm, and a speed of 15 r/min. The mean measured angle was 30.362° ± 2.457°. Table 8 lists the three comparison models, which differed in particle geometry and seed–seed rolling friction. Each model was run three times, with statistics based on the complete-revolution window defined in Section 2.5.

Table 8. Parameter settings of the three comparison models.

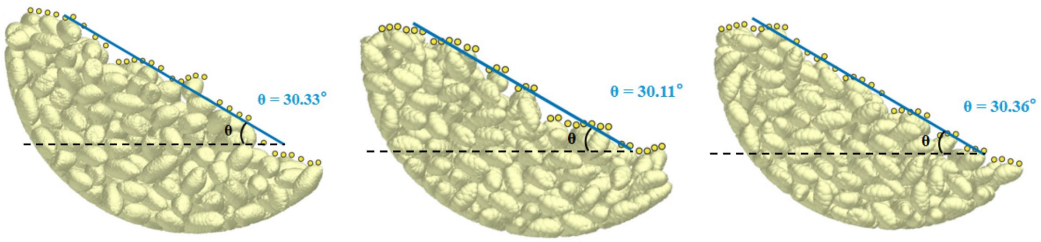
Model	Particle Geometry	Seed Allocation	Seed–Seed Rolling Friction	Seed–Wall Rolling Friction
CMG	Class-specific mean geometries	75, 150, 75	μ_0	0.12314
MGU	Weighted mean geometry	300	μ_0	0.12314
MGC	Weighted mean geometry	75, 150, 75	μ_{ij} (Table 7)	0.12314

CMG denotes the class-specific mean-geometry model; MGU, the mean-geometry model with uniform rolling friction; and MGC, the mean-geometry model with class-specific rolling friction. Geometries are defined in Section 2.3, and $\mu_0 = 0.02552$. MGC and MGU share the same geometry, but MGC assigns its 300 particles to classes in a 75:150:75 ratio. Same-class contacts use $\mu_i = \mu_0 K_i$; different-class contacts use Equation (9), with values in Table 7. Seed–wall rolling friction was obtained by inversion in Section 2.2.3.

Over 6.0–10.0 s, the dynamic angles were 30.317° ± 0.777° for CMG, 30.117° ± 0.451° for MGU, and 30.350° ± 0.458° for MGC, with relative errors of 0.15%, 0.81%, and 0.04%, respectively. One-way ANOVA did not detect a statistically significant difference among models ($p = 0.871$). The 0.233° range of model means was smaller than the 2.457° between-photograph SD of the measured response. MGU and MGC shared the same geometry and differed only in rolling friction assignment; Welch's test also did not detect a statistically significant difference for this pair. Thus, class-specific assignment redistributed resistance without a detectable change in the overall dynamic angle under this condition. This does not establish statistical equivalence. Table 9 summarizes the results. Figure 11 shows representative frames, with yellow markers indicating surface centroids and blue lines indicating fitted slopes. The angles derived from the frames in Figure 11 are frame-specific, whereas Table 9 reports means over one complete revolution.

Table 9. Dynamic angle-of-repose results for the three particle models.

Model	Mean (°)	Between-Replicate Standard Deviation (°)	95% Confidence Interval (°)	Relative Error (%)
CMG	30.317	0.777	28.387–32.246	0.15
MGU	30.117	0.451	28.996–31.237	0.81
MGC	30.350	0.458	29.212–31.488	0.04



(**a**) CMG (**b**) MGU (**c**) MGC

Figure 11. Granular beds and free-surface fits in the dynamic angle-of-repose simulations: (**a**) class-specific mean-geometry model (CMG); (**b**) mean-geometry model with uniform rolling friction (MGU); and (**c**) mean-geometry model with class-specific rolling friction (MGC).

3.4. EDEM–Fluent Coupling and Bench-Test Comparison

The vacuum peanut seed-metering device was tested on a JPS-12 bench (Harbin Bona Technology Co., Ltd., Harbin, China) at Jilin Agricultural University, and corresponding EDEM–Fluent simulations were conducted. The metering disc rotated at 19.5 r/min, the air-chamber vacuum level was 3.46 kPa, and the chamfered circular suction holes were 5.5 mm

in diameter. These conditions were selected from the design operating range reported by Yao [31]. Seeds came from the physical-property test batch, and physical tests and simulations used the 1:2:1 composition in Section 2.1. Two-way CFD–DEM coupling was implemented between Fluent and EDEM, with gas flow described in an Eulerian framework and seed motion resolved by DEM. Fluent computed the gas flow using the realizable k–ε turbulence model with standard wall functions. No-slip conditions were applied at all walls, with the metering-disc walls rotating and the stationary walls held fixed. EDEM computed seed motion and contacts using the Hertz–Mindlin (no slip) model and Standard Rolling Friction. Seed–gas drag was calculated using the Ergun–Wen–Yu drag model. Flow boundaries were calibrated against pressure measurements at the air-chamber-side end of each suction hole. Time-step synchronization and particle-conservation checks were applied to the coupled solution. Figure 12 shows the simulation and bench-test arrangements.



(**a**) Fluent simulation (**b**) EDEM simulation (**c**) Bench test

Figure 12. EDEM–Fluent coupled simulation and seed-metering bench test: (**a**) Fluent simulation; (**b**) EDEM simulation; and (**c**) bench test.

The Fluent time step and coupling exchange interval were both 53 μs. The EDEM contact time step was 20% of the Rayleigh time step, and the coupled model contained 300 seeds. Gas mass flow was monitored at the seed inlet, seed discharge outlet, and vacuum outlet; positive values indicate inflow and negative values outflow. Mean suction-hole pressure denotes the area-weighted pressure at the hole openings on the back of the metering disc. Absolute residual convergence criteria of 10^{-4} were set for continuity, the three velocity components, k, and ε, with a maximum of 50 iterations per physical time step.

Mesh sensitivity was assessed using four meshes containing 1,524,386, 2,181,047, 3,114,905, and 4,996,832 cells (Table 10). Mean suction-hole pressure and gas-phase mass flow rates at the three boundaries were compared. Relative to the finest mesh, the 3,114,905-cell mesh differed by 0.137%, 0.137%, 0.137%, and 0.044% in mean suction-hole pressure, seed-inlet gas mass flow rate, seed-discharge gas mass flow rate, and vacuum-outlet gas mass flow rate, respectively. Relative differences were calculated as the absolute difference divided by the absolute finest-mesh value. Refinement from 3,114,905 to 4,996,832 cells increased the cell count by 60.4%. The 3,114,905-cell mesh was therefore retained based on the comparison of these gas-phase quantities under the conditions examined here. The scope of this numerical check is discussed in Section 4.3.

Metering indices were determined according to GB/T 6973—2005, Testing Methods of Single Seed Drills (Precision Drills) [33]. The applicable technical requirements were those for the 10–20 cm theoretical spacing category in JB/T 10293—2013, Specifications for Single Seed Drills (Precision Drills) [34]. Simulation and bench testing each comprised five replicates, with 200 metering events recorded per replicate. The same event-classification rules and denominator were used to calculate all three indices. For each index, Table 11 reports

the mean, sample SD, and two-sided 95% t-based CI calculated as mean ± $t_{0.975,4}$ × SD/√5. Each simulation run or bench-test replicate was one statistical unit; the 1000 events per group were not treated as independent replicates. SDs are expressed in percentage points, and CI limits are percentages.

Table 10. Mesh-sensitivity comparison of mean suction-hole pressure and boundary gas-phase mass flow rates.

Cells	Mean Suction-Hole Pressure (Pa)	Seed-Inlet Gas Mass Flow (kg/s)	Seed-Discharge Gas Mass Flow (kg/s)	Vacuum-Outlet Gas Mass Flow (kg/s)
1,524,386	−1219.3	0.0124163	0.0068042	−0.0192188
2,181,047	−1229.4	0.0125174	0.0067489	−0.0192650
3,114,905	−1237.1	0.0125958	0.0067069	−0.0193018
4,996,832	−1238.8	0.0126131	0.0066977	−0.0193102

Table 11. Comparison of simulated and bench-test seeding indices.

Seeding Index	Requirement (%)	Simulation		Bench Test	
		Mean ± SD (%)	95% CI (%)	Mean ± SD (%)	95% CI (%)
Qualified	≥75	92.2 ± 1.440	90.411–93.989	92.1 ± 1.387	90.377–93.823
Multiple	≤20	6.7 ± 1.037	5.413–7.987	6.8 ± 1.151	5.371–8.229
Missed	≤10	1.1 ± 0.418	0.581–1.619	1.1 ± 0.418	0.581–1.619

The simulated qualified seeding index was 92.2%, compared with 92.1% in bench tests, a relative error of 0.11% (Table 11). Multiple seeding indices were 6.7% and 6.8%, respectively, with a relative error of 1.5%; both missed seeding indices were 1.1%. All three mean indices met the cited technical requirements. These comparisons support reproduction of overall metering performance for the tested batch and operating condition, without establishing predictive accuracy under other conditions.

4. Discussion

4.1. Calibration Results and Assessment of Simulation Accuracy

Static calibration produced a baseline seed–seed rolling friction coefficient of $\mu_0 = 0.02552$, which was redistributed among three seed classes using a shape relationship. This effective rolling friction coefficient was smaller than the measured static friction coefficient of 0.376. The two coefficients describe different resistance mechanisms and are not directly interchangeable. The ranking of the shape corrections matched the measured aspect ratios and critical angles. The fitted exponent, $p = 1.9446$, describes a more than proportional increase in the correction with aspect ratio within this dataset. This association is consistent with shape-dependent rolling and tumbling, but the fitted relationship does not identify the underlying contact-scale mechanisms.

The static rerun checked whether the calibrated coefficient reproduced the calibration target. The drum test compared simulated and measured dynamic angles, and the coupled simulation–bench comparison assessed overall metering performance under one operating condition. MGC and MGU produced similar dynamic angles, and Welch's test detected no statistically significant difference. The framework proposed by Pourandi et al. [21] suggests that the low-Froude-number drum condition may help explain the similar overall angles. Orefice et al. [22] likewise showed that a single free-surface measure does not describe the full flow state. Additional measures, such as particle velocity fields, would be needed to resolve class effects on internal motion. The present dynamic and bench comparisons

support the tested parameter assignment under the examined conditions; they do not establish its uniqueness or superior predictive accuracy relative to uniform rolling friction.

4.2. Practical Implications for Precision Peanut Seed-Metering Design

For the tested vacuum peanut seed meter, the results provide a basis for selecting particle representations and contact inputs. Static calibration determines the overall seed–seed rolling friction level, while the aspect-ratio corrections assign class differences without changing the weighted mean. The common geometry can thus be combined with class-specific rolling friction coefficients to represent the morphology-based classes in DEM. At 15 r/min, the mean-geometry model with class-specific friction produced a dynamic angle of 30.350° ± 0.458°, close to the CMG value of 30.317° ± 0.777°. This comparison informs model selection for the measured response. The maximum relative difference between simulated and measured mean metering indices was 1.5%. This comparison supports using these parameters to analyze the overall response of the tested device. Within the models and operating conditions examined here, the calibrated parameters can support analysis of candidate structural configurations of the current seed-metering device.

4.3. Limitations and Future Work

The study is limited to one Silihong peanut batch from one source, 4.18% wet-basis moisture content, the current multi-sphere representations, a drum speed of 15 r/min, and bench conditions of 19.5 r/min, 3.46 kPa vacuum, and 5.5 mm chamfered circular holes. Other cultivars, crops, batches, wall materials, or operating conditions require new measurements, calibration, and independent validation. Even a new batch of the same cultivar requires reassessment of moisture content, critical angles, static response, and baseline rolling friction; the present λ_0, p, and functional form of Equation (8) cannot be assumed to apply directly.

The geometries did not retain seed-coat irregularities, local contact curvature, or individual within-class variation. Wall elastic properties were provisional engineering values. Instrument and image-extraction uncertainties were not individually propagated into the reported CIs.

Sphere-count sensitivity was assessed only for the critical rolling angle over the tested counts, rather than for all responses or conditions. Run times were not compared across particle models, so their computational efficiency was not quantified.

The mesh-sensitivity assessment covered mean suction-hole pressure and three boundary gas-phase mass flow rates under the compared conditions. Because of computational cost, mesh independence was not assessed for particle-scale responses such as seed trajectories, attachment and release events, or seeding indices throughout the coupled process. Metering CIs describe variation among five replicates. The available tests do not establish parameter uniqueness, statistical equivalence, or predictive accuracy outside the tested conditions.

Future work will repeat calibration across batches, moisture levels, and cultivars to assess whether p and λ_0 remain appropriate. Dynamic evaluation will include particle velocity fields, and bench validation will cover additional rotational speeds, vacuum levels, and suction-hole configurations.

5. Conclusions

Physical and contact properties were measured for the upper, middle, and lower Silihong peanut seed classes. Mean lengths were 15.15, 14.03, and 13.94 mm, respectively, and the mean seed density was 1018.2 kg m^{-3}. A 29-sphere mean geometry was constructed from a representative seed whose dimensions were closest to the 1:2:1-weighted mean

dimensions. Inversion of the static angle-of-repose response gave a baseline seed–seed rolling friction coefficient of $\mu_0 = 0.02552$. An aspect-ratio power law with $p = 1.9446$ yielded shape corrections of 1.1046, 0.9687, and 0.9579 while preserving the weighted mean coefficient. Multiplication by the baseline gave class-specific coefficients of 0.02819, 0.02472, and 0.02445. Rerunning the static simulation with the calibrated coefficient reproduced the calibration target with a relative error of 0.485%. At 15 r/min, the corrected and uncorrected mean-geometry models produced similar dynamic angles. A one-way ANOVA did not detect a statistically significant difference among the three models ($p = 0.871$). Relative errors for the qualified, multiple, and missed seeding indices against JPS-12 bench tests were 0.11%, 1.5%, and 0%, respectively, and the mean indices met JB/T 10293—2013 requirements. These results provide a case-specific reference for the tested Silihong batch, moisture content, particle representation, and metering condition. The procedure can inform subsequent crop-specific research, but transferability across cultivars, crops, or operating conditions has not been established.

Author Contributions: All authors contributed to developing the research approach. W.F.: conceptualization and writing—original draft; X.J.: writing—review and editing; X.O.: formal analysis and writing—review and editing; C.L.: formal analysis and writing—review and editing; M.L.: formal analysis and writing—review and editing; D.H.: formal analysis and writing—review and editing; G.W.: formal analysis and writing—review and editing; D.F.: writing—review and editing; W.S.: writing—review and editing; J.W.: formal analysis and writing—review and editing. All authors have read and agreed to the published version of the manuscript.

Funding: This research received no external funding.

Data Availability Statement: The original contributions presented in this study are included in the article. Further inquiries can be directed to the corresponding author.

Conflicts of Interest: The authors declare no conflicts of interest.

Abbreviations

DEM	Discrete element method
CFD	Computational fluid dynamics
CMG	Class-specific mean-geometry model
MGU	Mean-geometry model with uniform rolling friction
MGC	Mean-geometry model with class-specific rolling friction
ANOVA	Analysis of variance
SD	Standard deviation
CI	Confidence interval

References

1. National Bureau of Statistics of China. *China Statistical Yearbook 2024*; China Statistics Press: Beijing, China, 2024. (In Chinese)
2. Fang, Z.; Liu, P. Source of China's three major oilseeds production capacity increases. *Chin. J. Oil Crop Sci.* **2025**, *47*, 243–259. (In Chinese with English abstract) [CrossRef]
3. Cundall, P.A.; Strack, O.D.L. A discrete numerical model for granular assemblies. *Géotechnique* **1979**, *29*, 47–65. [CrossRef]
4. Tsuji, Y.; Kawaguchi, T.; Tanaka, T. Discrete particle simulation of two-dimensional fluidized bed. *Powder Technol.* **1993**, *77*, 79–87. [CrossRef]
5. Wensrich, C.M.; Katterfeld, A. Rolling friction as a technique for modelling particle shape in DEM. *Powder Technol.* **2012**, *217*, 409–417. [CrossRef]
6. Coetzee, C. Calibration of the discrete element method: Strategies for spherical and non-spherical particles. *Powder Technol.* **2020**, *364*, 851–878. [CrossRef]
7. Li, Y.; Tian, X.; Zhao, Y.; Liu, X.; Zhou, M.; Dai, F.; Wang, W. Parameter calibration and experiment of polyhedral cottonseed discrete element based on Tavares model. *Trans. Chin. Soc. Agric. Mach.* **2024**, *55*, 124–131. (In Chinese with English abstract) [CrossRef]

8. Ding, X.; Wang, B.; He, Z.; Shi, Y.; Li, K.; Cui, Y.; Yang, Q. Fast and precise DEM parameter calibration for *Cucurbita ficifolia* seeds. *Biosyst. Eng.* **2023**, *236*, 258–276. [CrossRef]
9. Wang, S.; Lu, M.; Liu, X.; Ji, J.; Chen, P. Calibration and analysis of discrete element simulation parameters of Chinese cabbage seeds. *PLoS ONE* **2022**, *17*, e0270415. [CrossRef] [PubMed]
10. Hao, J.; Wei, W.; Huang, P.; Qin, J.; Zhao, J. Calibration and experimental verification of discrete element parameters for oil sunflower seeds. *Trans. Chin. Soc. Agric. Eng.* **2021**, *37*, 36–44. (In Chinese with English abstract) [CrossRef]
11. Wang, L.; Yang, H.; Wang, Z.; Wang, Q.; Lu, C.; Wang, C.; He, J. Calibration of DEM polyhedron model for wheat seed based on angle of repose test and semi-resolved CFD-DEM coupling simulation. *Agriculture* **2025**, *15*, 506. [CrossRef]
12. Yang, L.; Chen, W.; Kan, Z.; Meng, H.; Qi, J. Parameter calibration for discrete element simulation of *Leymus chinensis* seeds based on RSM optimization. *Sci. Rep.* **2025**, *15*, 7947. [CrossRef] [PubMed]
13. Zhang, S.; Tekeste, M.Z.; Li, Y.; Gaul, A.; Zhu, D.; Liao, J. Scaled-up rice grain modelling for DEM calibration and the validation of hopper flow. *Biosyst. Eng.* **2020**, *194*, 196–212. [CrossRef]
14. Mousaviraad, M.; Tekeste, M.Z. Systematic calibration and validation approach for discrete element method (DEM) modeling of corn under varying moisture contents (MC). *J. ASABE* **2024**, *67*, 259–274. [CrossRef]
15. Long, S.; Zhang, Y.; Kang, S.; Li, B.; Wang, J. Parameter calibration of the angle of repose of particle materials based on convolutional neural network. *Biosyst. Eng.* **2024**, *245*, 152–163. [CrossRef]
16. Kodicherla, S.P.K.; Nandyala, D.K. Morphological effects on the angle of repose of granular materials: A discrete element investigation. *Granul. Matter* **2023**, *25*, 71. [CrossRef]
17. Doan, T.; Indraratna, B.; Nguyen, T.T.; Rujikiatkamjorn, C. Interactive role of rolling friction and cohesion on the angle of repose through a microscale assessment. *Int. J. Geomech.* **2023**, *23*, 04022250. [CrossRef]
18. Wang, H.; Wu, P.; He, H.; Ma, Y.; Bu, K.; Xue, J. Calibration of parameters for discrete element simulation model for alfalfa with different moisture contents based on angle of repose test. *BioResources* **2022**, *17*, 1467–1484. [CrossRef]
19. Xu, T.; Yu, H.; Huang, D.; Yu, Y.; Li, C.; Gou, Y.; Wang, J. Modeling of olive fruit based on discrete element method and analysis of the sensitivity of Young's modulus parameters. *Trans. Chin. Soc. Agric. Eng.* **2025**, *41*, 175–182. (In Chinese with English abstract) [CrossRef]
20. Du, X.; Liu, C.; Liu, C.; Sun, Q.; Chen, S. A novel method for measurement of the angle of repose of granular seeds in discrete element methods. *J. Agric. Eng.* **2023**, *54*, 1504. [CrossRef]
21. Pourandi, S.; van der Sande, P.C.; Weinhart, T.; Ostanin, I. A mathematical model for the dynamic angle of repose of a granular material in the rotating drum. *Powder Technol.* **2024**, *446*, 120176. [CrossRef]
22. Orefice, L.; Remmelgas, J.; Neveu, A.; Francqui, F.; Khinast, J.G. A novel methodology for data analysis of dynamic angle of repose tests and powder flow classification. *Powder Technol.* **2024**, *435*, 119425. [CrossRef]
23. Xu, J.; Sun, S.; He, Z.; Wang, X.; Zeng, Z.; Li, J.; Wu, W. Design and optimisation of seed-metering plate of air-suction vegetable seed-metering device based on DEM-CFD. *Biosyst. Eng.* **2023**, *230*, 277–300. [CrossRef]
24. Sun, W.; Yi, S.; Qi, H.; Li, Y.; Dai, Z.; Zhang, Y.; Yuan, J.; Wang, S. DEM-CFD coupling simulation and optimization of an air-pressure high-speed precision seed-metering device for maize delta-row dense plantings. *Powder Technol.* **2025**, *466*, 121481. [CrossRef]
25. Xing, H.; Cao, X.; Zhong, P.; Wan, Y.; Lin, J.; Zang, Y.; Zhang, G. DEM-CFD coupling simulation and optimisation of rice seed particles seeding a hill in double cavity pneumatic seed metering device. *Comput. Electron. Agric.* **2024**, *224*, 109075. [CrossRef]
26. Lei, X.; Zhu, P.; Deng, X.; Li, M.; Chen, Y.; Ren, W. Seed motion and airflow characteristics in a centralized pneumatic seed-metering device for rice using CFD-DEM coupled approach and bench testing. *Powder Technol.* **2026**, *469*, 121884. [CrossRef]
27. Wang, Y.; Su, W.; Lai, Q.; Lin, Y.; Li, J. Simulation and measurement of the suction force on ellipsoidal seeds in an air-suction seed-metering device. *Biosyst. Eng.* **2023**, *232*, 97–113. [CrossRef]
28. Guo, P.; Sun, B.; Shang, S.; Hou, J.; Wang, D.; Zhao, Z.; Elshafie, A.; Zheng, X.; Eltoum, F. Effect of auxiliary air-suction seed-filling structure on seed discharge performance of peanut high-speed seed-metering machine. *Agriculture* **2025**, *15*, 1678. [CrossRef]
29. Diao, H.; Ye, W.; Zhang, Z.; Liu, X.; Zhao, Z.; Zeng, F.; Li, X.; Cui, J.; Liu, Y. Measurement of the physical parameters of peanut seeds and calibration of the discrete element parameters. *INMATEH Agric. Eng.* **2024**, *72*, 444–453. [CrossRef]
30. Wu, M.; Cong, J.; Yan, Q.; Zhu, T.; Peng, X.; Wang, Y. Calibration and experiments for discrete element simulation parameters of peanut seed particles. *Trans. Chin. Soc. Agric. Eng.* **2020**, *36*, 30–38. (In Chinese with English abstract) [CrossRef]
31. Yao, K. Design and experimental study of air suction peanut precision seeder. Master's Thesis, Jilin Agricultural University, Changchun, China, 2024. (In Chinese with English abstract)
32. Nakata, Y.; Moriguchi, S.; Kajiyama, S.; Kido, R.; Kikkawa, N.; Saomoto, H.; Takano, D.; Higo, Y. Experimental data of 3D printed granular material for verification of discrete element modeling simulation. *Soils Found.* **2022**, *62*, 101178. [CrossRef]

33. *GB/T 6973—2005*; Testing Methods of Single Seed Drills (Precision Drills). Standards Press of China: Beijing, China, 2005. (In Chinese)
34. *JB/T 10293—2013*; Specifications for Single Seed Drills (Precision Drills). China Machine Press: Beijing, China, 2013. (In Chinese)

Disclaimer/Publisher's Note: The statements, opinions and data contained in all publications are solely those of the individual author(s) and contributor(s) and not of MDPI and/or the editor(s). MDPI and/or the editor(s) disclaim responsibility for any injury to people or property resulting from any ideas, methods, instructions or products referred to in the content.